Pharm Res (2012) 29:1366–1379
DOI 10.1007/s11095-012-0681-0

RESEARCH PAPER

A Model for Predicting Field-Directed Particle Transport in the Magnetofection Process

Edward P. Furlani • Xiaozheng Xue

Received: 5 August 2011 / Accepted: 6 January 2012 / Published online: 14 February 2012

ABSTRACT

Purpose To analyze the magnetofection process in which magnetic carrier particles with surface-bound gene vectors are attracted to target cells for transfection using an external magnetic field and to obtain a fundamental understanding of the impact of key factors such as particle size and field strength on the gene delivery process.

Methods A numerical model is used to study the field-directed transport of the carrier particle-gene vector complex to target cells in a conventional multiwell culture plate system. The model predicts the transport dynamics and the distribution of particle accumulation at the target cells.

Results The impact of several factors that strongly influence gene vector delivery is assessed including the properties of the carrier particles, the strength of the field source, and its extent and proximity relative to the target cells.

Conclusions The study demonstrates that modeling can be used to predict and optimize gene vector delivery in the magnetofection process for novel and conventional *in vitro* systems.

KEY WORDS magnetic biotransport · magnetic gene delivery · magnetic targeting · magnetofection · magnetophoresis

E. P. Furlani · X. Xue
Dept. Chemical & Biological Engineering
University at Buffalo (SUNY)
614 Furnas Hall
Buffalo, New York 14260-4200, USA

E. P. Furlani (✉)
Dept. of Electrical Engineering, University at Buffalo (SUNY)
614 Furnas Hall
Buffalo, New York 14260-4200, USA
e-mail: efurlani@buffalo.edu

INTRODUCTION

Magnetic particles are finding increasing use in emerging applications in fields that include microbiology, nanomedicine and biotechnology where they are routinely used to sort and separate biomaterials. A key motivation for using magnetic particles is that they can be functionalized to selectively bind to (magnetically label) target biomaterials, thereby enabling noninvasive control of such materials using a magnetic field (1–5). Magnetic particles can be synthesized in sizes that range from a few nanometers to microns with a narrow size distribution, which makes them ideal for manipulating biomaterials such as proteins (5−50 nm), viruses (20−450 nm), genes (2 nm wide and 10−100 nm long), or whole cells (10–100 μm) (2–4). Furthermore, the most commonly used particles, typically made from magnetite Fe_3O_4, are nontoxic and well-tolerated by living organisms when properly synthesized and functionalized. Specifically, magnetic particles can be custom-tailored with appropriate surface treatments that enhance biocompatibility and enable coating with affinity biomolecules for highly specific binding with a target biomaterial. Magnetic particles that are sufficiently small (nanoscale) exhibit a unique superparamagnetic behavior. i.e. they are easily magnetized by an applied magnetic field, but return to an unmagnetized state instantaneously when the field is removed (5). Superparamagnetic particles experience a magnetic force when their induced dipole moment couples to a local field gradient, but this force vanishes when the field is turned off. Moreover, magnetically labeled biomaterial in a carrier fluid can be efficiently and selectively controlled using an external field because such fluids typically have a low intrinsic magnetic susceptibility, which makes them in effect transparent to the magnetic field.

The field-induced transport of magnetically labeled biomaterial enables accelerated delivery to a target tissue, which greatly reduces process time as compared to diffusion-limited transport. Magnetic particle transport is leveraged in the process of magnetofection where magnetic carrier particles with surface-bound gene vectors are attracted towards target cells for transfection (6–16). In a conventional *in vitro* magnetofection system a multiwell culture plate is used, wherein the target cells are at the bottom of each well, and an array of rare-earth magnets, aligned beneath the wells provides the magnetic force that attracts the particle-gene vector complex towards the cells as shown in Fig. 1b. Magnetofection has distinct advantages over other transfection methods (16). Specifically, high transfection rates can be achieved with significantly lower vector doses and the process time is dramatically reduced, from hours to minutes. However, despite these advantages, few authors have modeled field-directed particle transport and accumulation for this process (17–19).

In this paper numerical models are presented for analyzing the magnetofection process in multiwell systems. These models include a particle transport model and closed-form equations for predicting the magnetic field and force. The transport model involves the numerical solution of a drift-diffusion equation that governs the spatio-temporal behavior of the particle concentration. It is used to study transport dynamics and particle accumulation within a well. The transport equation takes into account fluidic, magnetic and gravitational forces on the particles as well as Brownian dynamics. It is solved numerically using the finite volume method (FVM) with boundary conditions that mimic the magnetofection process. The magnetic force used in the transport equation. is obtained in closed-form, which simplifies the analysis and greatly enhances computational speed and accuracy as compared to purely numerical field analysis. A separate analysis of the magnetic field and force reveals interesting features of their spatial distributions that depend on the orientation of magnetization in the source magnets (Fig. 1a). An analysis of the force distribution within a well indicates that it not only attracts particles downwards towards the base, but it also focuses particles towards the center of the well during transport. The magnetic force controls the rate and distribution of particle accumulation, and can be optimized by choosing appropriate particle properties, chamber dimensions and spacing between the magnet and the well.

MATERIALS AND METHODS

The models developed in this paper are demonstrated via application to a conventional 96 well plate magnetofection system. In this system the well plate is positioned above a magnet plate that contains an array of cylindrical magnets, aligned with the wells as shown in Fig. 1b. The well chambers are flat bottomed with somewhat tapered walls and have a mean inner radius and height of R_c=3.3 mm and height L_c=10.9 mm, respectively. The wall thickness is approximately 1 mm and the wells are spaced 9 mm apart, center-to-center (Greiner Bio-One Microplates, www.greinerbioone.com). The magnets are made from Neodymium Iron Boron (NdFeB). They have a radius R_m=3 mm, a length L_m=5 mm, and are magnetized to

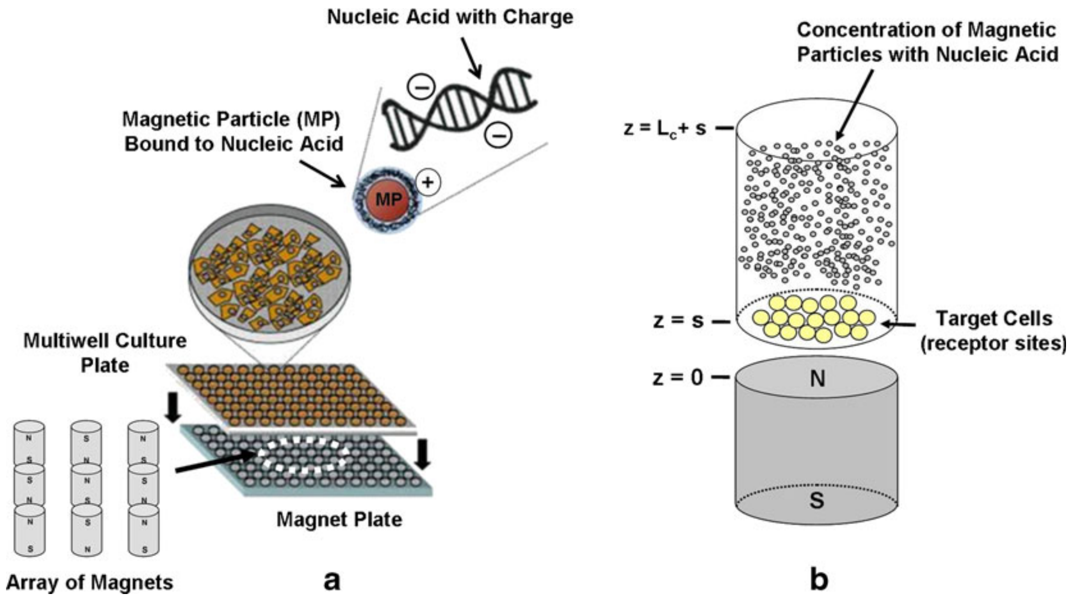

Fig. 1 Multiwell plate magnetofection system: (**a**) array of cell cultures positioned above an array of cylindrical magnets (adapted from (6)), (**b**) the magnetic force pulls magnetic nanoparticles with surface bound gene vectors towards the cells.

saturation, $M_s = 9.55 \times 10^5 \mathrm{A/m}(B_r = 1.2\ T)$ (magnet NE65 from IBS Magnet, www.ibsmagnet.com). The top of the magnets are nominally approximately 1–2 mm beneath the inside bottom of their respective well chambers.

Particle Transport Equation

The motion of colloidal magnetic particles in a magnetic field is governed by various factors including magnetic and fluidic forces, buoyancy, Brownian dynamics, interparticle effects (notably magnetic dipole-dipole interactions) and momentum transfer from the particles to the fluid (17–31). In the following analysis the particle concentration is assumed to be sufficiently dilute so that interparticle effects and particle-to-fluid momentum transfer can be neglected. Particle transport is modeled using a drift-diffusion equation that governs the particle volume concentration $c(t)$ (17–19,21–28),

$$\frac{\partial c}{\partial t} + \nabla \bullet \mathbf{J} = 0 \tag{1}$$

where $\mathbf{J} = \mathbf{J}_D + \mathbf{J}_F$ is the total flux of particles, which includes a contribution $\mathbf{J}_D = -D\nabla c$ due to diffusion, and a contribution due to the drift of the particles $\mathbf{J}_F = Uc$, which is due to the action of forces. Here, $D = \mu kT$, k is Boltzmann's constant, T is temperature in Kelvin, η is the fluid viscosity. The particle mobility is given by $\mu = 1/(6\pi\eta R_{p,hyd})$ where $R_{p,hyd}$ is the effective hydrodynamic radius of the particle, which takes into account particle-bound biomaterial. $\mathbf{U}$ is the particle drift velocity given by $\mathbf{U} = \mathbf{v}_\mathrm{f} + \mu\left(\mathbf{F}_\mathrm{m} + \mathbf{F}_\mathrm{g}\right)$ where $\mathbf{v}_\mathrm{f}$ is the fluid velocity and $\mathbf{F}_\mathrm{m}$ and $\mathbf{F}_\mathrm{g}$ are the external magnetic and gravitational forces on the particles. Note that in the absence of external forces, $\mathbf{U} = \mathbf{v}_\mathrm{f}$, which implies that the particles move with the same velocity as the fluid. However, in the magnetofection process, the fluid is stationary $\mathbf{v}_\mathrm{f} = 0$, and therefore $\mathbf{U} = \mu\left(\mathbf{F}_\mathrm{m} + \mathbf{F}_\mathrm{g}\right)$. It should also be noted that the gravitational force is usually negligible compared to the magnetic force for submicron particles.

Magnetic Force

The magnetic force on a particle is computed using the "effective" dipole moment method in which the particle is modeled as an "equivalent" point dipole with an effective moment $\mathbf{m}_\mathrm{p,eff}$ (17–19,28). The force on the dipole (and hence on the particle) is given is given by

$$\mathbf{F}_\mathrm{m} = \mu_f\left(\mathbf{m}_\mathrm{p,eff} \bullet \nabla\right)\mathbf{H}_\mathrm{a} \tag{2}$$

where μ_f is the permeability of the fluid, and $\mathbf{H}_\mathrm{a}$ is the applied magnetic field intensity at the center of the particle, were the equivalent point dipole is located. The moment $\mathbf{m}_\mathrm{p,eff}$ can be determined using a magnetization model that takes into account self-demagnetization and magnetic saturation of the particles (17–20,28–32), i.e.

$$\mathbf{m}_\mathrm{p,eff} = V_p f(\mathrm{H_a})\mathbf{H}_\mathrm{a} \tag{3}$$

where

$$f(H_a) = \begin{cases} \frac{3(\chi_p - \chi_f)}{(\chi_p - \chi_f)+3} & H_a < \left(\frac{(\chi_p - \chi_f)+3}{3\chi_p}\right)M_{sp} \\ M_{sp}/H_a & H_a \geq \left(\frac{(\chi_p - \chi_f)+3}{3\chi_p}\right)M_{sp} \end{cases} \tag{4}$$

Here, $V_p = \frac{4}{3}\pi R_p^3$ is the volume of the particle, χ_p and χ_f are the magnetic susceptibilities of the particle and fluid, respectively, and M_{sp} is the saturation magnetization of the particle. Thus, the magnetic force can be rewritten as

$$\mathbf{F}_\mathrm{m} = \mu_f V_p f(H_a)(\mathbf{H}_\mathrm{a} \bullet \nabla)\mathbf{H}_\mathrm{a}. \tag{5}$$

This can be determined once an expression for $\mathbf{H}_\mathrm{a}$ is known. Analytical and closed-form field expressions for both a single cylindrical magnet with uniform axial magnetization and an array of such magnets are given in the Appendix.

Solution Method

The drift-diffusion equation (Eq. 1) is solved numerically using the FVM. For this method, the computational domain, in this case a well chamber, is discretized into a set of computational nodes and cells, wherein each cell is centered about a node. One-dimensional (1D) and two-dimensional (2D) transport models are used for the analysis. The 1D model, which neglects the radial dependence of the field, is computationally efficient and ideal for performing rapid parametric studies of particle accumulation as a function of variables such as the particle size and magnet-to-well-spacing. Moreover, despite its limitations, the 1D model provides insight into the transport dynamics. The 2D model, which accounts for both radial and axial dependencies, provides a detailed description of the spatio-temporal distribution of particle concentration throughout a well as well as the accumulation of particles on its base.

In the 1D model the FVM discretization of Eq. 1 at an interior node is

$$c_i^{n+1} = c_i^n + \frac{\delta t}{\delta z}\left(F_{i+1/2} - F_{i-1/2}\right)(i = 1, 2, \ldots, N_z) \tag{6}$$

where $\delta z = L_c/N_z$ is the length of a computational cell and L_c is the length of the well as shown in Fig. 1b. Here, c_i^n and c_i^{n+1} are the values of the concentration at the i'th computational node at time steps n and n+1, respectively (17). $F_{i\pm1/2}$ is a discretized representation of the particle flux $D\frac{\partial c}{\partial z} - Uc$ at the edges of the computational cell $z_{i\pm1/2}$, and is computed using an upwind numerical scheme,

$$F_{i+1/2} = D\frac{c_{i+1}^n - c_i^n}{\delta z} - \left(\min(U_i, 0)c_i^n + \max(U_{i-1}, 0)c_{i-1}^n\right). \qquad (7)$$

Note that the corresponding particle flux (i.e. the number of particles passing through a unit area at $z_{i+1/2}$ per second) is $F_{p,i+1/2} = F_{i+1/2}/V_p$. As for the boundary conditions, let $z_{c,t}$ and $z_{c,b}$ represent the coordinates of the top and bottom of the well, respectively, and let s denote the spacing between the top of the magnet and the bottom of the well as shown in Fig. 1b. The closed-form field solutions presented in the Appendix, i.e. Equations A1 and A7, apply when the magnet is positioned with its top surface is at $z = 0$, and therefore $z_{c,t} = L_c + s$ and $z_{c,b} = s$ as shown in Fig. 1b. Equation 6 is solved subject to an initial condition, which specifies a uniform concentration of particles throughout the well, i.e. $c(z, 0) = c_0$. A Neumann boundary condition is imposed at the top of the well and a Dirichlet condition $c(z_{c,b}, t) = 0$ is imposed at the bottom. The former reflects the fact that no particles cross the top of the well, i.e. there is zero flux at this boundary. The latter boundary condition mimics the magnetofection process wherein particles that reach the base of the well are assumed to bind with receptor sites on the target cells, and therefore are removed from the computational domain so that they no longer effect the transport dynamics. It is assumed that there are a sufficient number of receptors to accommodate all of the particles in the well. The particle accumulation on the cells is computed as a cumulative sum of the number of particles that reach the base of the well during each time step.

For the 2D model the system is assumed to be axisymmetric. While this is true for a single isolated magnet, it amounts to a simplifying approximation for a magnet in the array because the field and force contributions from neighboring magnets vary with the angular position relative to the magnet. Nevertheless, the approximation is reasonable because the angular variation due to neighboring magnets is small. Thus, the 2D field distribution can be used for analysis as shown below.

The drift-diffusion equation for the 2D analysis is

$$\frac{\partial c}{\partial t} = \frac{1}{r}\frac{\partial}{\partial r}\left(r\left(D\frac{\partial c}{\partial r} - U^r c\right)\right) + \frac{\partial}{\partial z} \times \left(D\frac{\partial c}{\partial z} - U^z c\right), \qquad (8)$$

where U^r and U^z are drift velocities in r and z directions, respectively (17). The computational domain is $0 \leq r \leq R_c$ and $z_{c,b} \leq z \leq z_{c,t}$ where R_c is the radius of chamber, and $z_{c,b}$ and $z_{c,t}$ are as above. The FVM discretization of Eq. 8 at an interior node (i,j) is as follows

$$c_{i,j}^{n+1} = c_{i,j}^n + \delta t \times \left(\frac{1}{r_i}\frac{r_{i+1/2}F_{i+1/2,j} - r_{i-1/2}F_{i-1/2,j}}{\delta r} + \frac{G_{i,j+1/2} - G_{i,j-1/2}}{\delta z}\right) \qquad (9)$$

where $F_{i\pm1/2,j}$ and $G_{i,j\pm1/2}$ denote the particle flux through the edges of the computational cell perpendicular to the r and z axis, respectively. Equation 8 is solved with Neumann (zero-flux) boundary conditions imposed at the top ($z = z_{z,t}$) and outer edge ($r = R_c$) of the well, and a Dirichlet condition $c(r, z_{c,b}, t) = 0$ imposed at its base to mimic the accumulation of particles on the cells, as described in the 1D case.

RESULTS

The transport models are used to analyze magnetofection in a conventional 96 well plate system. Throughout this analysis the particles are assumed to be magnetite (Fe_3O_4), which has a density $\rho_p = 5{,}000\ \mathrm{kg/m^3}$ and saturation magnetization $M_{sp} = 4.78 \times 10^5\mathrm{A/m}$. To simplify the analysis, the particles are assumed to have a hydrodynamic radius equal to their physical radius, $R_{p,hyd} = R_p$. A magnetization model is adopted that is consistent with Eq. 4 when $\chi_p >> 1$, i.e. (28),

$$f(H_a) = \begin{cases} 3 & H_a < M_{sp}/3 \\ M_{sp}/H_a & H_a \geq M_{sp}/3 \end{cases}. \qquad (10)$$

This model applies to superparamagnetic nanoparticles, but is used here as simplifying approximation for somewhat larger submicron particles. The fluid is assumed to have the same properties as water, i.e. nonmagnetic $\chi_f = 0$, with a viscosity $\eta = 0.001\ \mathrm{N{\cdot}s/m^2}$, and a density $\rho_f = 1{,}000\ \mathrm{kg/m^3}$. Before studying particle transport, it is useful to first model the magnetic field and force in the system as these provide an intuitive understanding of the transport dynamics. The formulas in the Appendix are used for this analysis.

Single Magnet Analysis

It is instructive to analyze the field and force due to a single isolated magnet before studying a multiwell system. As noted above, each NdFeB magnet has a radius R_m=3 mm, length L_m = 5 mm and a magnetization $M_s = 9.55 \times 10^5\mathrm{A/m}$. Throughout this section, a reference frame is chosen such that the top surface of the magnet is located at z = 0 as shown in Fig. 1b. The magnetic field and force are computed using Eqs. A1 and A2. As a first step, the axial field B_z and its gradient $\frac{dB_z}{dz}$ are computed from the top of the magnetic upward along the z-axis ($0 \leq z \leq 7$ mm) as shown in Fig. 2. Note that near the base of the well (z=1.5 mm), $B_z \approx 260$ mT and $\frac{dB_z}{dz} \approx 125\,\mathrm{T/m}$. However, these decay rapidly with distance from the magnet as shown. Since the magnetic force is proportional to the product of these variables it also decays with distance, which implies that more efficient accumulation will be realized if the particles are initially introduced into a lower portion of a well, instead of being uniformly dispersed throughout the entire well.

Next, radial and axial force components on a Fe_3O_4 particle with R_p=100 nm are computed using Eqs. A4 and A5 at various distances above the magnet along a line that spans the diameter of the magnet as shown in Fig. 3. It should be noted that the force profiles are axisymmetric and plotted as a function of normalized distance x/R_m from the center of the magnet. Note also that the force is on the order of femto-Newtons, however it can be substantially increased by choosing larger particles as it scales with R_p^3. In a previous study, similar force plots were erroneously labeled using pico-Newtons instead of femto-Newtons (see Fig. 2 in reference (17)). The axial force F_{mz} is negative and acts to attract particles downward towards the surface of the magnet as indicated by the vertical arrow in Fig. 3a. Note that at greater distances from the magnet, F_{mz} is strongest along the z-axis. However, closer to the magnet, F_{mz} obtains its maximum value at a radial distance away from the axis. This implies that the particles will tend to accumulate in an annular region at the bottom of the well. The radial force F_{mr} obtains a maxium negative value above the radial edge of the magnet. This force directs particles radially inward towards the z-axis, away from the edge as indicated by the horizontal arrows shown in Fig. 3b. This will act to produce a higher particle accumulation towards the center of the well with minimal accumulation near the edge of the magnet. The distribution of accumulated particles is examined in the transport analysis below.

Magnet Array Analysis

The field and force profiles above an array of magnets can be computed using the principle of superposition as described in the Appendix. It is instructive to consider the field in a culture well located in the interior of the array. Since

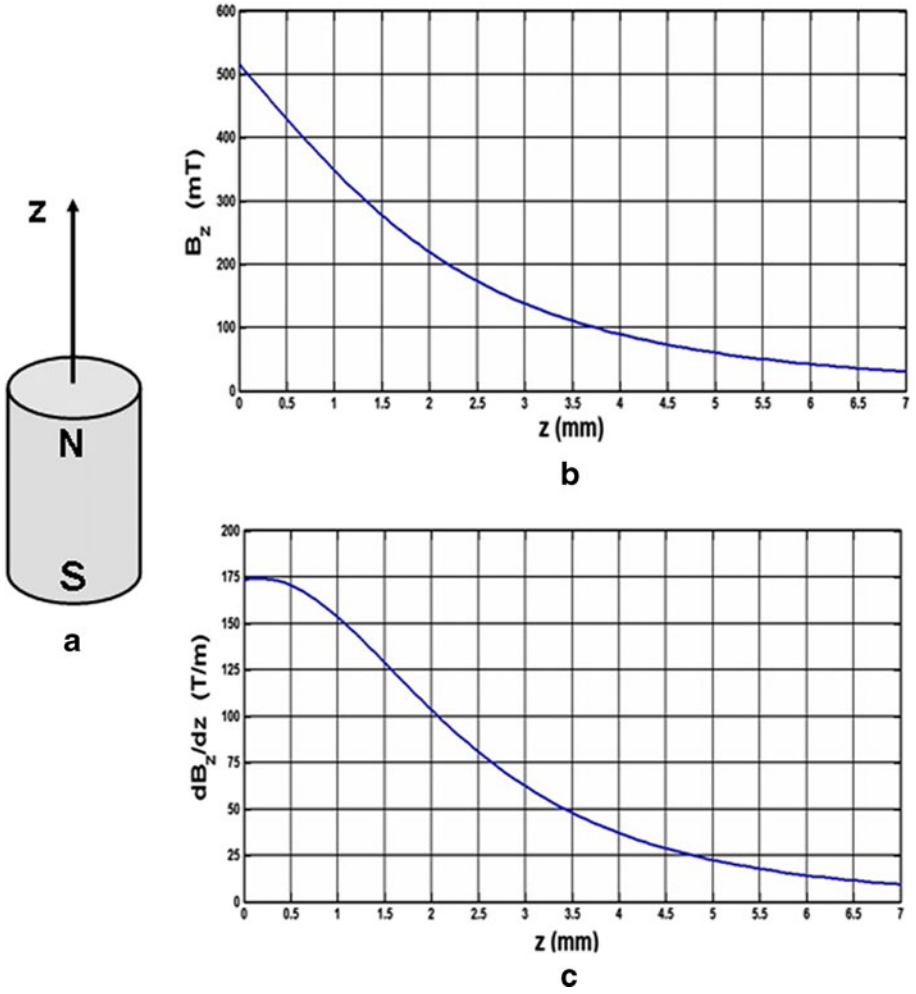

Fig. 2 Axial field and gradient above a cylindrical rare-earth magnet: (**a**) magnet and reference frame (**b**) B_z, and (**c**) $\frac{dB_z}{dz}$.

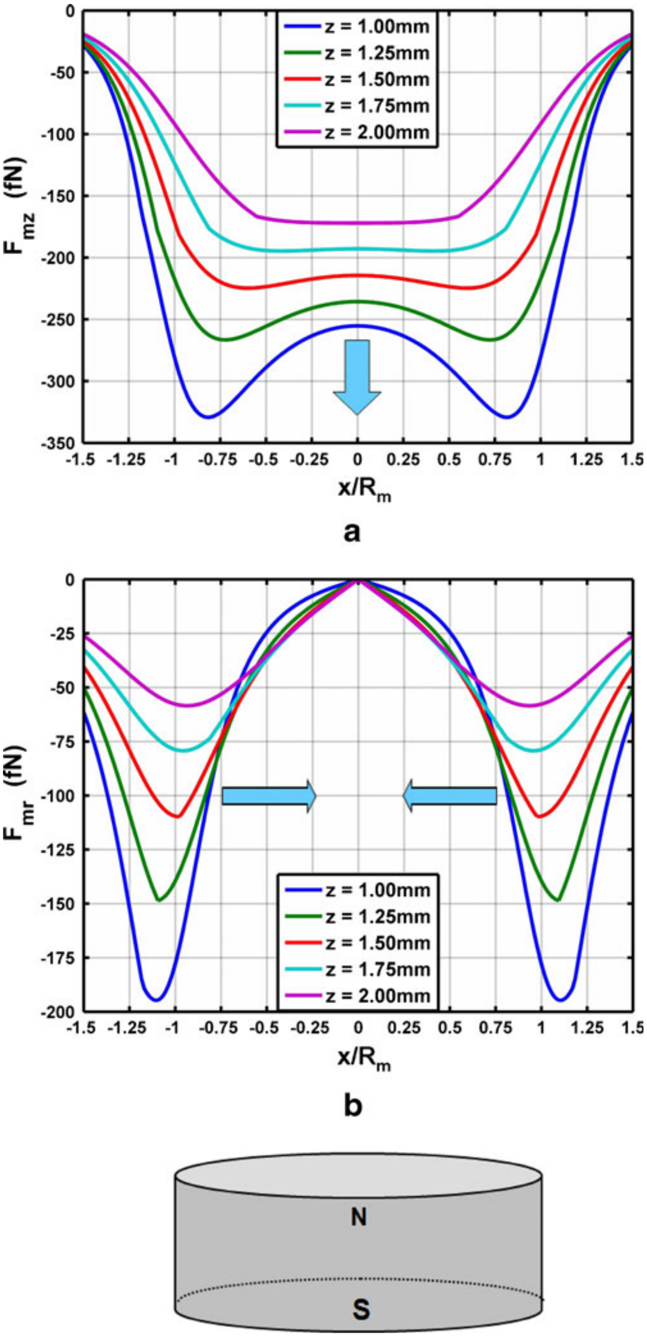

Fig. 3 Magnetic force above a rare-earth magnet: (**a**) F_{mz}, (**b**) F_{mr}.

the field of an individual magnet decays relatively rapidly with distance, one can study the field inside the well by superimposing the field of the magnet beneath the well with the fields of the nearest neighbor magnets. Thus, it suffices to consider a sub-array of 9 magnets consisting of a central magnet, which is beneath the well, and its nearest neighbors as shown in Fig. 4. The field inside a well on the perimeter of the array can be analyzed in a similar fashion, but it will have contributions from fewer magnets. For the interior well analysis, two different magnetization orientations are considered; unidirectional magnetization (not shown) in which all the magnets are magnetized upward, and alternating magnetization in which neighboring magnets have antiparallel magnetization as shown in Fig. 4. The field and force for these orientations is computed at a distance z = 1 mm above the array, which is in close proximity to the cells at the bottom of the well. Surface plots of the components B_z and F_{mz} are shown in Figs. 5 and 6, respectively, and corresponding contour plots of F_{mz} are shown in Fig. 7. Note that these plots exhibit substantially axisymmetric profiles as discussed above. A more direct comparison of the field and force for the two orientations is shown in Fig. 8 where corresponding variables are plotted together as a function of normalized distance x/R_m from the center of the magnet. This analysis shows that the alternating magnetization configuration as shown in Fig. 4 produces a stronger axial magnetic force within the well. Thus, this configuration should produce more rapid and efficient transfection as compared to the unidirectional configuration. This is illustrated in greater detail in the transport analysis below. An analysis was also performed to study the effect of reducing the distance between neighboring wells and magnets. The results showed that the wells could be placed much closer together without compromising the magnetic force or transfection efficiency.

Particle Transport Analysis

The particle transport study begins with a 1D drift-diffusion analysis of particle accumulation at the base of a well as a function of the separation *s* between the base and the top of the magnet: *s* = 0.5, 1.0, 1.5, 2.0, and 2.5 mm (Fig. 1b). Since a magnet array with alternating magnetization produces a

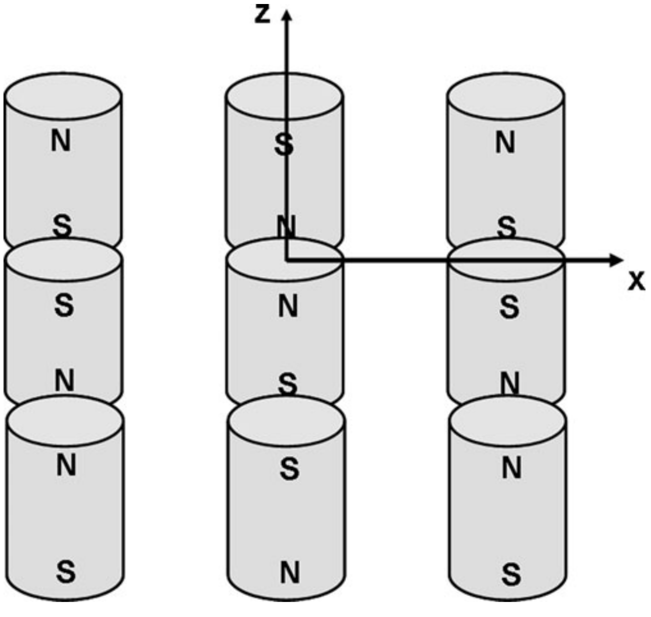

Fig. 4 Array of magnets with alternating magnetization.

Fig. 5 Surface plots of B_z at z= 1 mm above an array of magnets: (**a**) uniform upward magnetization, (**b**) alternating nearest neighbor magnetization.

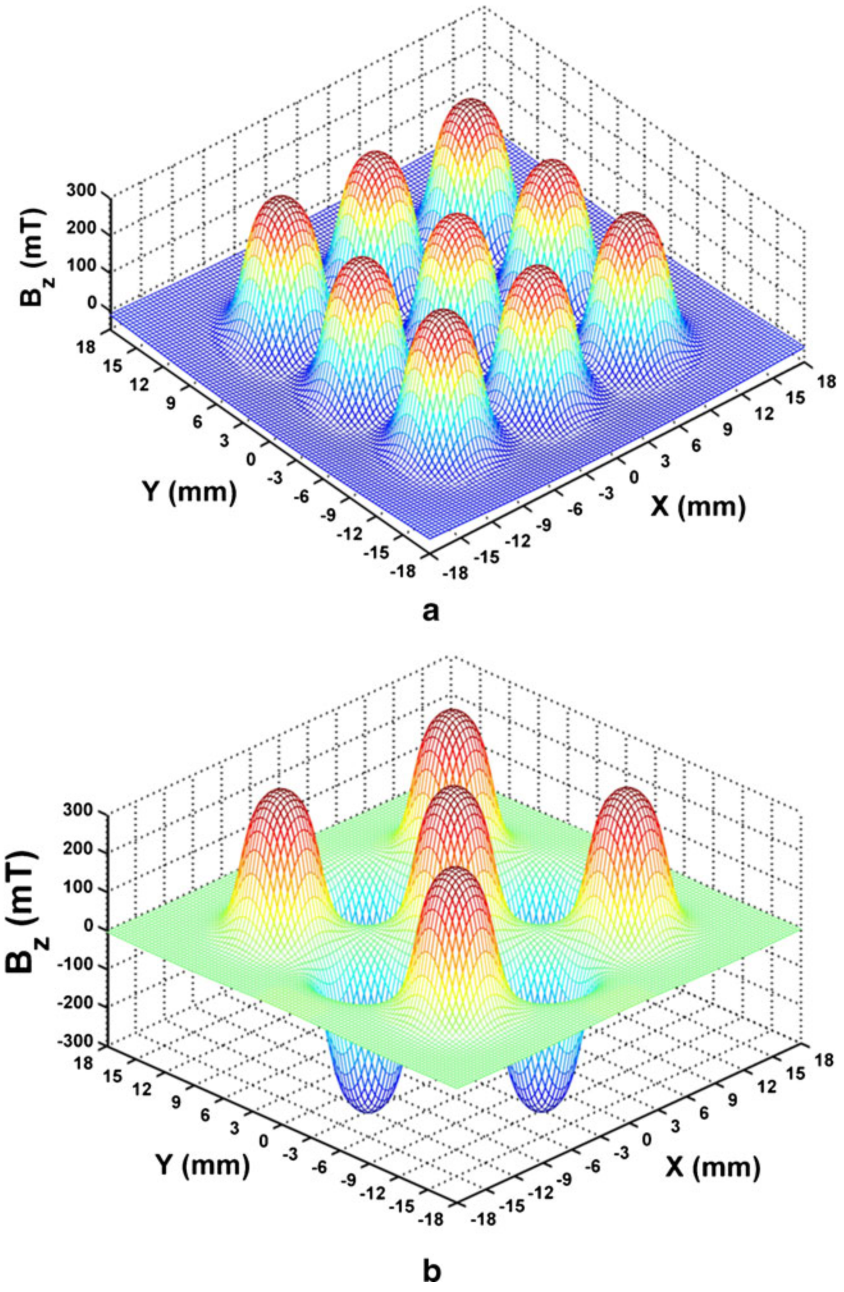

stronger axial force, the 1D study is performed using the field in the central well of that array. It is assumed that there is a uniform concentration (c_o = 0.001) of colloidal Fe_3O_4 particles (R_p = 100 nm) occupying a volume 6 mm high in the well. Note that this implies that the particles occupy only a fraction of the well, which has a height of 10.9 mm. The rate of particle accumulation at the base of the well is shown in Fig. 9. Note that for the nominal well-to-magnet separation, s = 1 mm, the majority (90%) of the total initial number of particles have accumulated at the base of the well within 1,200 s (20 min). By comparison, the predicted diffusion-limited accumulation during this time (not shown), which is obtained by solving the transport equation with the magnetic force set to zero, is less than 1%. Thus, magnetic field-induced particle accumulation can be orders of magnitude faster than diffusion-limited accumulation, as has been observed (33). Moreover, the accumulation rate can be increased by decreasing the well-to-magnet spacing.

Next, the 2D drift-diffusion model is applied to predict the distribution of accumulated particles at the base of a well. The analysis is performed using the field distribution in the center well of an alternating magnetization array (Fig. 4). The radial distribution of the percentage of accumulated particles per unit area (%/mm^2) is shown

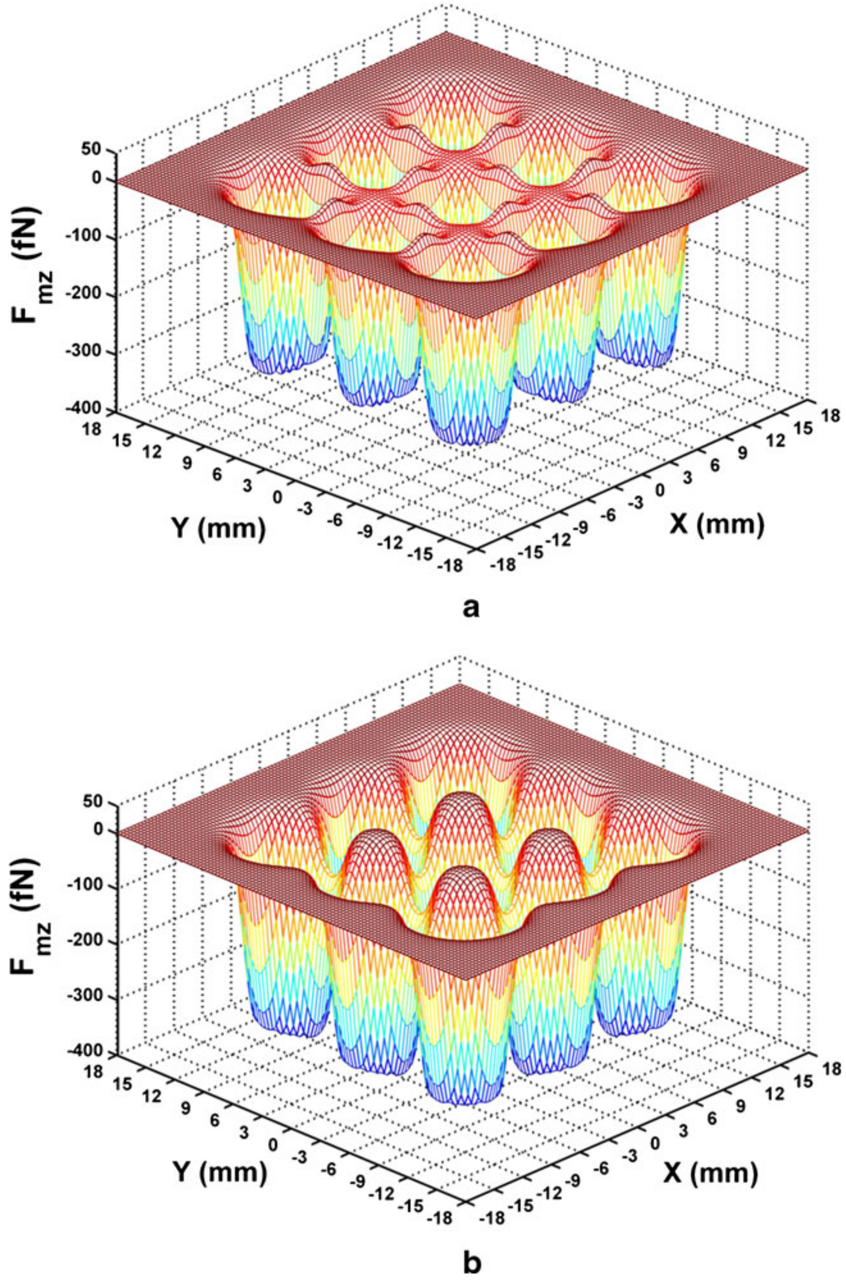

Fig. 6 Surface plots of F_z at z= 1 mm above an array of magnets: (**a**) uniform upward magnetization, (**b**) alternating nearest neighbor magnetization.

in Fig. 10a. This distribution is relatively constant up to the mid radius of the chamber $r/R_c = 0.5$, but decreases rapidly thereafter. This is due in part to the radial field-directed focusing of the particles during transport as described above. This analysis is important because it implies that more efficient transfection should occur near the center of the well where particle accumulation is greatest. Thus, standard multi-well plates, where the well radius is comparable or greater than the underlying magnet radius, are not optimal for magnetofection as the cells positioned towards the outer region of the well will experience less efficient transfection. This is confirmed by plotting the percent of total particle accumulation *vs.* radial distance as shown in Fig. 10b. This plot indicates that a majority of the particles accumulate near the center of the well, i.e. away from its outer wall, which in this case is aligned with the edge of the magnet. Thus, a higher transfection efficiency can be achieved when the well has a smaller radius than the magnet in which case all of the cells would then be positioned within a region of relatively high particle accumulation. This analysis demonstrates the key advantages of the 1D and 2D transport models, notably, they provide physical insight into the factors governing particle accumulation, and they

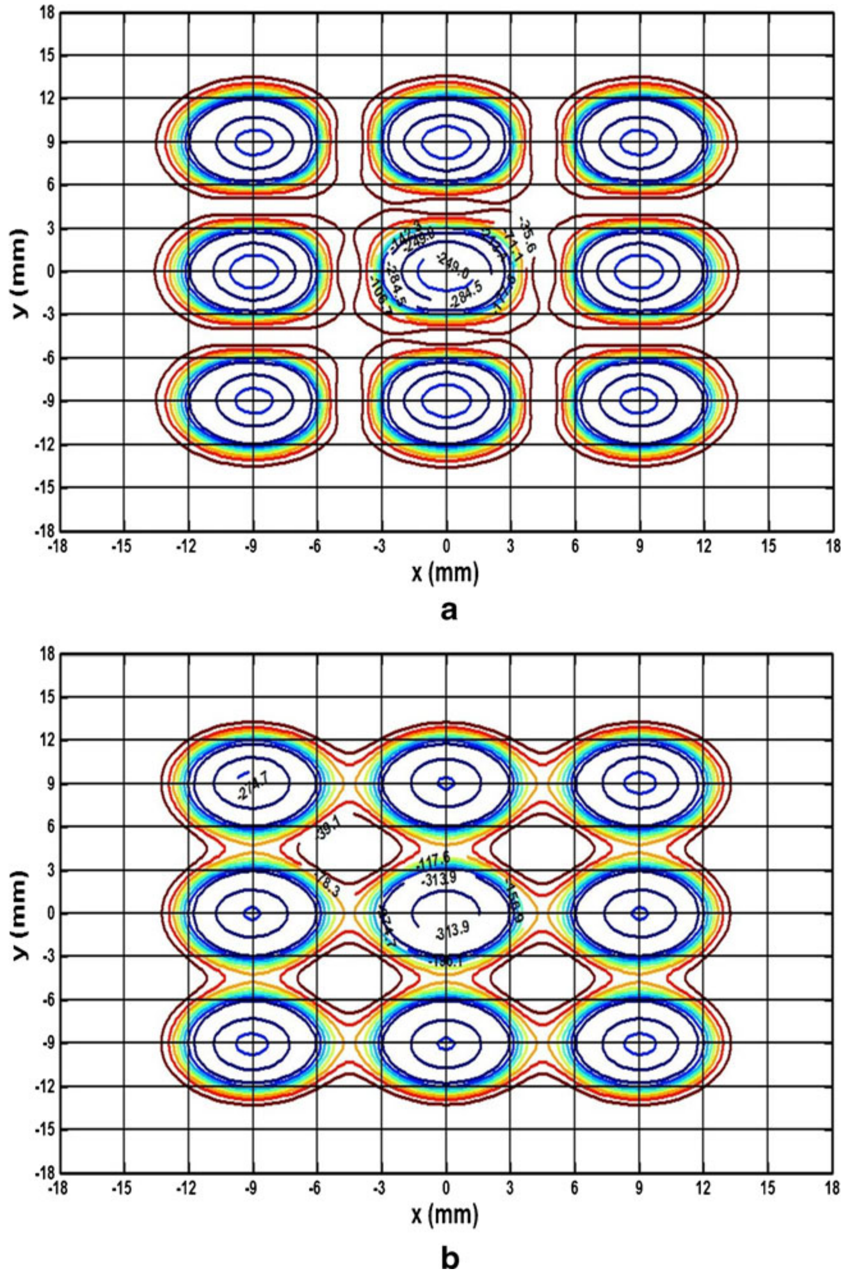

Fig. 7 Contour plots of F_z at z= 1 mm above a magnet array: (**a**) uniform upward magnetization, (**b**) alternating nearest neighbor magnetization.

can be used to design and optimize novel magnetofection systems prior to fabrication.

DISCUSSION

The modeling described above reveals many interesting features of multiwell systems that impact magnetofection performance. One such feature is that a stronger downward directed (axial) magnetic force is obtained inside a well when its neighboring magnets have an alternating magnetization as shown in Fig. 4, as compared to unidirectional magnetization. Another interesting feature is that the radial component of the magnetic force focuses particles towards the center of a well as shown in Fig. 3b. This is manifest in the particle distribution at the base of a well, which clearly shows higher accumulation near the center as shown in Fig. 10a. Thus, it should be possible to achieve more efficient transfection with smaller samples by using wells with smaller radii than their corresponding magnets.

The transport analysis clearly shows that field-directed particle accumulation can be orders of magnitude faster than diffusion-limited accumulation, as observed in practice. Furthermore, the rate of accumulation increases as the magnet-to-chamber spacing decreases because the magnetic force is stronger closer to the magnet. Thus, the transfection

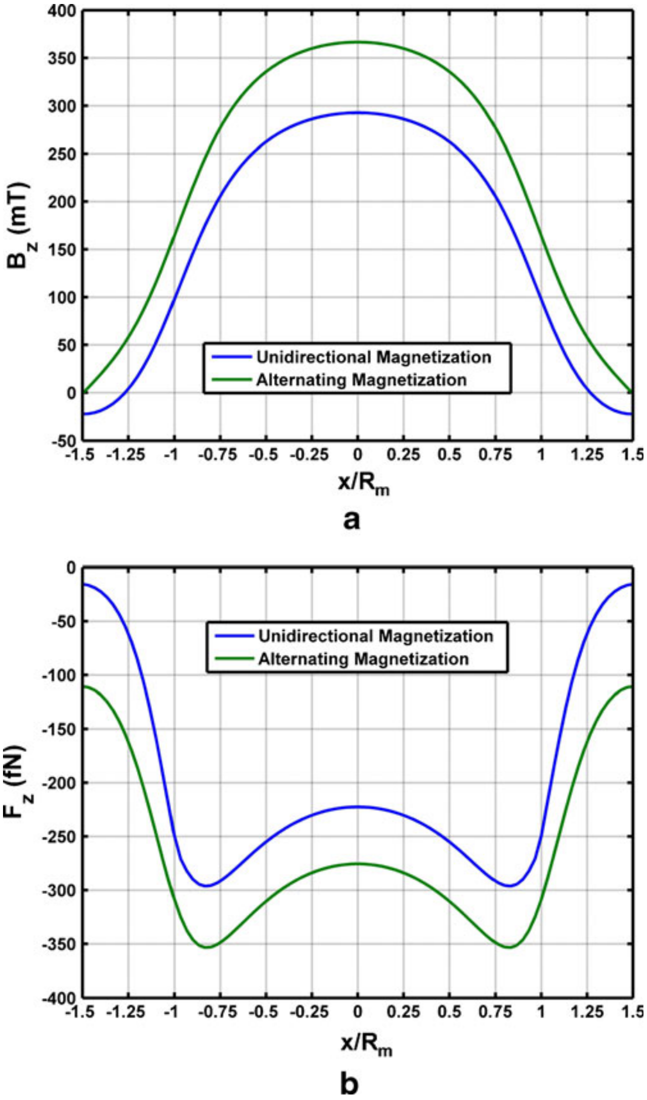

Fig. 8 Comparison of B_z and F_z for uniform and alternating magnetization at z=1 mm above the central magnet: (**a**) B_z, and (**b**) F_z.

rate and efficiency could be optimized by reducing this spacing as well.

CONCLUSION

Models have been presented for analyzing magnetofection in multiwell plate systems. These include 1D and 2D particle transport models and closed-form equations for predicting the magnetic field and force. The transport models can be used to study the spatio-temporal behavior of the particle concentration within a well and to predict the distribution of accumulated particles at the base of a well where the cells are located and transfection takes place. The models have been demonstrated via application to a conventional 96 well plate magnetofection system. Together, these models enable a fundamental understanding of particle transport and accumulation in the magnetofection process. They are relatively easy to implement and enable the design and optimization of novel magnetofection systems.

ACKNOWLEDGMENTS & DISCLOSURES

The authors are grateful to Professor Christian Plank and Dr. Olga Mykhaylyk for many useful technical discussions.

APPENDIX

In this section, closed-form formulas are presented for predicting the magnetic field and force in multiwell plate magnetofection systems. The field for these systems is produced by an array of cylindrical rare-earth magnets positioned beneath the multiwell plate as shown in Fig. 1a. The field distribution above the magnet array can be obtained by superimposing the fields of the constituent magnets and the force is easily computed given the field. In the following, both 1D (on axis) and 2D field and force solutions are given for a single isolated magnet. The superposition of the 2D field solutions for the array is briefly discussed.

Single Magnet Field Analysis

Two different field and force solutions are given for a single magnet; simplified 1D (on axis) solutions, and more general 2D solutions. The 1D solutions are analytical and ideal for estimating the magnitude and decay of the field and force with distance, and for studying parametric dependencies. The 2D solutions are in closed-form and are evaluated using semi-numerical analysis.

The 1D Field and Force

In the 1D analysis, all radial dependence is neglected, and the magnetic field and force vectors are assumed to be strictly in the z-direction, i.e. no radial components. This approximation provides useful intuitive predictions when the culture well is much smaller than the magnet i.e. when the magnet diameter is much greater than the dimensions (diameter and height) of the well. The 1D axial field solution for a cylindrical rare-earth magnet that is magnetized to saturation M_s along its axis is given by (see p 129 in (34)),

$$H_z(z) = \frac{M_s}{2}\left[\frac{z+L_m}{\sqrt{(z+L_m)^2+R_m^2}} - \frac{z}{\sqrt{z^2+R_m^2}}\right], \tag{A1}$$

where z is the distance above the top of the magnet, and L_m and R_m are the length and radius of the magnet,

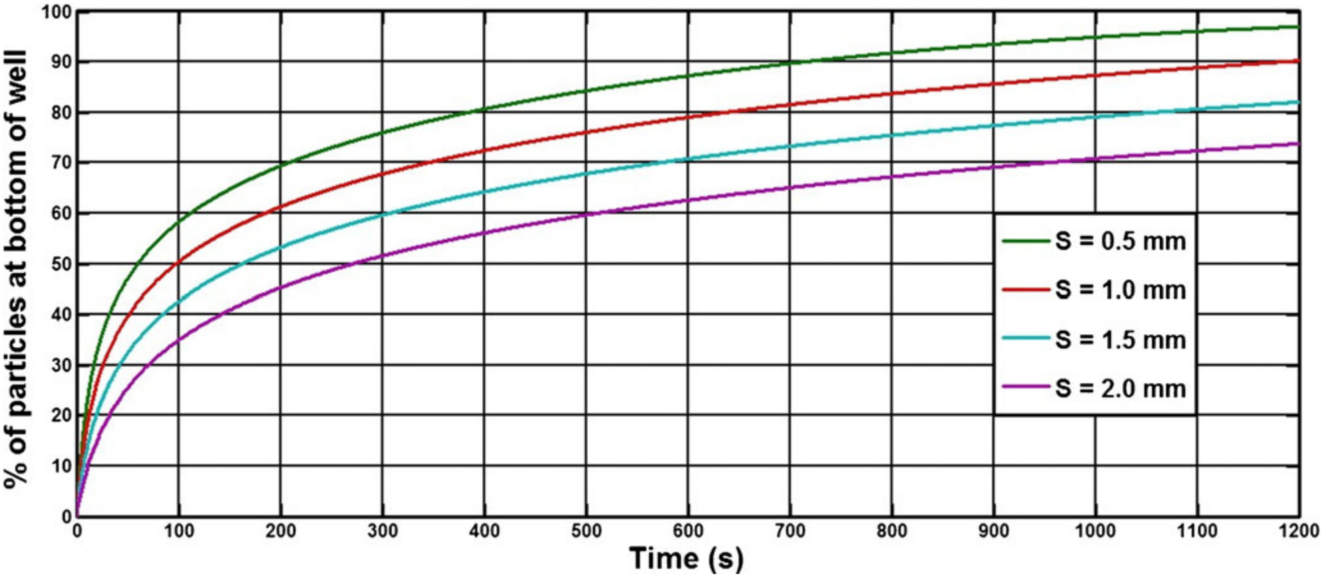

Fig. 9 Particle accumulation:% of particles accumulated at the base of a well chamber *vs*. time as a function of magnet-to-chamber spacing s.

respectively. In this approximation, the force on a particle with a volume V_p is

$$F_{mz}(z) = \mu_0 V_p f(H_\mathrm{a}) \frac{M_s^2 R_m^2}{4}\left[\frac{(z+L_m)}{\left((z+L_m)^2+R_m^2\right)^2} + \frac{z}{\left(z^2+R_m^2\right)^2} - \frac{(z+L_m)\left((z+L_m)^2+R_m^2\right)+z\left(z^2+R_m^2\right)}{\left(z^2+R_m^2\right)^{3/2}\left((z+L_m)^2+R_m^2\right)^{3/2}}\right]. \tag{A2}$$

The 2D Field and Force

In the 2D analysis both the radial and axial force components are computed,

$$\mathbf{F}_m(r,z) = F_{mr}(r,z)\,\hat{r} + F_{mz}(r,z)\,\hat{z}, \tag{A3}$$

where

$$F_{mr}(r,z) = \mu_0 V_p f(\mathrm{H_a}) \times \left[H_r(r,z)\frac{\partial H_r(r,z)}{\partial r} + H_z(r,z)\frac{\partial H_r(r,z)}{\partial z}\right], \tag{A4}$$

$$F_{mz}(r,z) = \mu_0 V_p f(\mathrm{H}) \times \left[H_r(r,z)\frac{\partial H_z(r,z)}{\partial r} + H_z(r,z)\frac{\partial H_z(r,z)}{\partial z}\right], \tag{A5}$$

and

$$\mathbf{H}_a = H_{ar}(r,z)\,\hat{r} + H_{az}(r,z)\,\hat{z}. \tag{A6}$$

The field $\mathbf{H}_\mathrm{a}$ is needed to determine the force. To obtain this, the magnet is modeled as equivalent current source as described in section 3.3 of (34), additional useful models for rare-earth magnet structures can be found in (35–38). A cylindrical magnet with a uniform axial magnetization produces the same external field as that of a conventional surface current that flows around the cylindical circumference of the magnet. The field distribution due to the magnet can be obtained via superposition, wherein the "equivalent" surface current is discretized into a finite set of current loop elements, and the total field is obtained by summing the field contributions from the individual elements. The field solution for a current loop is known (see p 263 in (39)). If the magnet is magnetized to saturation M_s, and centered about the z-axis with its top surface at $z = 0$, its field is given by

$$H_{ar}(r,z) = \frac{M_s}{2\pi}\int_{-L_m}^{0} \Pi_r(r,z,z')\,dz' \tag{A7}$$

$$H_{az}(r,z) = \frac{M_s}{2\pi}\int_{-L_m}^{0} \Pi_z(r,z,z')\,dz',$$

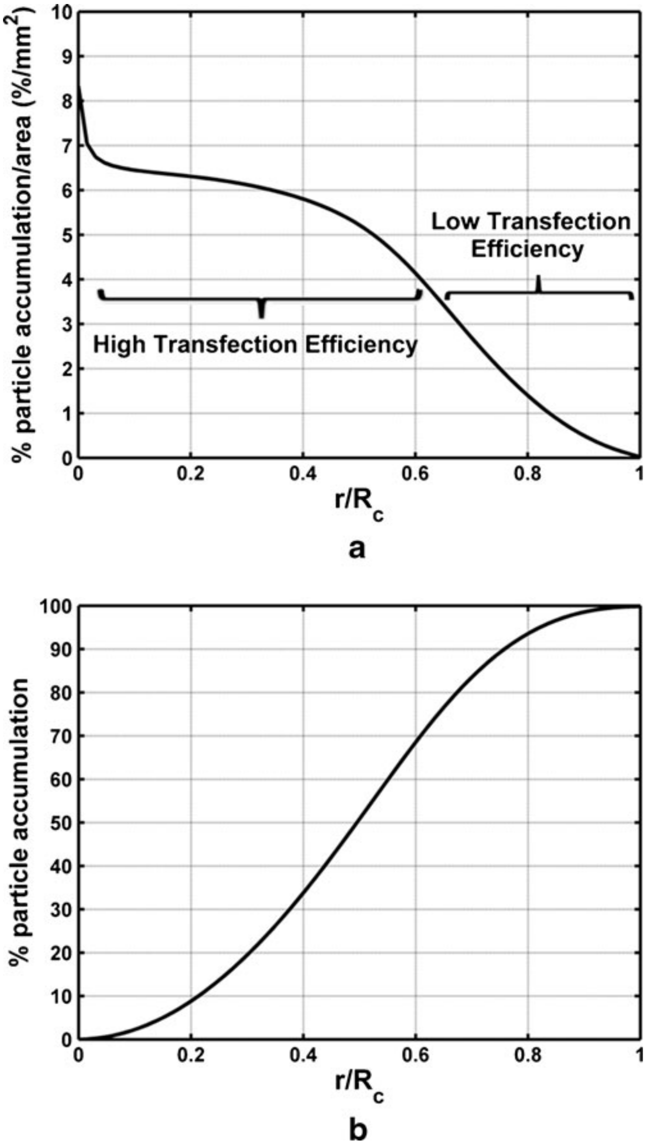

Fig. 10 Distribution of particle accumulation at the base of a well: (**a**)% particle accumulation per area (**b**) cumulative% particle accumulation.

where

$$\Pi_r(r,z,z') = \frac{(z-z')f(z,z')}{r}\left[R_t\left(z,z'\right)E(k) - K(k)\right], \tag{A8}$$

and

$$\Pi_z(r,z,z') = f(z,z')[Z_t(z,z')E(k) + K(k)]. \tag{A9}$$

In these expressions $K(k)$ and $E(k)$ are the complete elliptic integrals of the first and second kind, respectively (40),

$$K(k) = \int_0^{\frac{\pi}{2}} \frac{1}{\sqrt{1-k^2\sin^2(\phi)}}\,d\phi, \qquad E(k) = \int_0^{\frac{\pi}{2}} \sqrt{1-k^2\sin^2(\phi)}\,d\phi \tag{A10}$$

and

$$d = (R_m - r)^2 + \delta(z,z')^2,\; f(z,z') = \frac{1}{\left((R_m+r)^2 + \delta(z,z')^2\right)^{1/2}},$$

$$k = \left(\frac{4rR_m}{(R_m+r)^2 + \delta(z,z')^2}\right)^{1/2},\; R_t(z,z') = \frac{R_m^2 + r^2 + \delta(z,z')^2}{d},$$

$$Z(z,z') = \frac{R_m^2 - r^2 - \delta(z,z')^2}{d}, \delta(z,z') = (z - z'). \tag{A11}$$

The field components (A7) are computed using numerical integration. To evaluate the force, the gradient of the field needs to be determined. After considerable analysis and simplification one obtains,

$$\frac{\partial H_r(r,z,z')}{\partial r} = -\left(\frac{1}{r} + (R_m + r)f^2\right)\prod\nolimits_r + \frac{(z-z')f}{r} \times \left[\frac{\partial R_t}{\partial r}E(k) + \frac{\partial k}{\partial r}(R_t dE(k) - dK(k))\right] \tag{A12}$$

$$\frac{\partial H_r(r,z,z')}{\partial z} = \frac{f^2(R_m+r)^2}{z-z'}\prod\nolimits_r + \frac{(z-z')f}{r} \times \left[\frac{\partial R_t}{\partial z}E(k) + \frac{\partial k}{\partial z}(R_t dE(k) - dK(k))\right] \tag{A13}$$

$$\frac{\partial H_z(r,z,z')}{\partial r} = -f^2(R_m + r)\prod\nolimits_z + f\left[\frac{\partial Z_t}{\partial r}E(k) + \frac{\partial k}{\partial r}(Z_t dE(k) + dK(k))\right] \tag{A14}$$

$$\frac{\partial H_z(r,z,z')}{\partial z} = -f^2\left(z-z'\right)\prod\nolimits_z + f\left[\frac{\partial Z_t}{\partial z}E(k) + \frac{\partial k}{\partial z}(Z_t dE(k) + dK(k))\right] \tag{A15}$$

The magnetic force is computed by substituting (A7)–(A15) into Eqs. A4 and A5 and integrating over the length of the magnet as in Eq. A7.

Array of Magnets

The magnetic field and force due to an array of cylindrical magnets can be obtained by superimposing the fields of the constituent magnets. Let N be the total number of magnets in the array, and let n = 0,1,2,3,4, …, N-1 identify the constituent magnets. Choose a reference frame in which the central magnet, which is labeled $n = 0$, is located at the origin in the x-y plane as shown in Fig. 3. The field components of this magnet in cylindrical coordinates is given by Eq. A7. These need to be carefully converted to Cartesian coordinates to implement the superposition. The field solution for this magnet in Cartesian coordinates at an arbitrary observation point (x,y,z) is denoted by,

$$\begin{aligned}&\mathbf{H}_a^{(0)}(x,y,z)\\&\quad= H_{ax}^{(0)}(x,y,z)\hat{x} + H_{ay}^{(0)}(x,y,z)\hat{y} + H_{az}^{(0)}(x,y,z)\hat{z}\end{aligned} \qquad \text{(A16)}$$

The n'th magnet in the array is centered at $x = x_n$ and $y = y_n$ in the x-y plane. The field components for this magnet can be written in terms of the field of the 0'th magnetic as follows:

$$\begin{aligned}&\mathbf{H}_a^{(n)}(x,y,z) = \mathbf{H}_a^{(0)}(x - x_n, y - y_n, z)\\&\quad(n = 1, 2, 3, \ldots, N)\end{aligned} \qquad \text{(A17)}$$

The total field distribution of the array is obtained by summing the field contributions from all the magnets,

$$\mathbf{H}_a(x,y,z) = \sum_{n=0}^{N-1} \mathbf{H}_{ax}^{(n)}(x - x_n, y - y_n, z) \qquad \text{(A18)}$$

Finally, the total magnetic force on a particle of volume V_p due the array of magnets is given by

$$\mathbf{F}_\mathrm{m} = \mu_f V_p f(H_a)(\mathbf{H}_\mathrm{a} \bullet \nabla)\mathbf{H}_\mathrm{a} \qquad \text{(A19)}$$

where $\mathbf{H}_\mathrm{a}$ is obtained using Eq. A18.

REFERENCES

1. Marcucci F, Lefoulon F. Active targeting with particulate drug carriers in tumor therapy: fundamentals and recent progress. Drug Discov Today. 2004;9(5):219–28.
2. Pankhurst QA, Thanh NKT, Jones SK, Dobson J. Progress in applications of magnetic nanoparticles in biomedicine. J Phys D: Appl Phys. 2009;42:224001.
3. Hafeli U, Schutt W, Teller J (Eds.). 1997 Scientific and clinical applications of magnetic carriers. New York: Plenum Press; 1997.
4. Berry CC. Progress in functionalization of magnetic nanoparticles for applications in biomedicine. J Phys D: Appl Phys. 2009;42:224003.
5. Furlani EP. Magnetic biotransport: analysis and applications. Materials. 2010;3(4):2412–46.
6. Plank C, Zelphati OF, Mykhaylyk O. Magnetically enhanced nucleic acid delivery. Ten years of magnetofection-Progress and prospects. Adv Drug Deliv Rev. 2001;63(14–15):1300–31.
7. Plank C, Schillinger U, Scherer F, Bergemann C, Rémy J-S, Krötz F, Anton M, Lausier J, Rosenecker J. The magnetofection method: using magnetic force to enhance gene delivery. Biol Chem. 2003;384:737–47.
8. Scherer F, Anton M, Schillinger U, Henke J, Bergemann C, Kruger A, Gansbacher B, Plank C. Magnetofection: enhancing and targeting gene delivery by magnetic force *in vitro* and *in vivo*. Gene Ther. 2002;9:102–9.
9. Plank C, Anton M, Rudolph C, Rosenecker J, Krötz F. Enhancing and targeting nucleic acid delivery by magnetic force. Expert Opin Biol Ther. 2003;3:745–58.
10. Plank C, Scherer F, Schillinger U, Bergemann C, Anton M. Magnetofection: enhancing and targeting gene delivery with superparamagnetic nanoparticles and magnetic fields. J Liposome Res. 2003;13(1):29–32.
11. Plank C, Scherer F, Schillinger U, Anton M. Magnetofection: enhancement and localization of gene delivery with magnetic particles under influence of a magnetic fields. J Gene Med. 2000;2((5) Suppl):S24.
12. Plank C. Magnetofection: enhancing and targeting gene delivery with lipid-DNA vectors by magnetic force. J Liposome Res. 2003;13(1):105–6.
13. Krötz F, Son HY, Gloe T, Planck C. Magnetofection potentiates gene delivery to cultured endothelial. J Vasc Res. 2003;40:425–34.
14. Krötz F, Wit C, Sohn HY, Zahler S, Gloe T, Pohl U, Plank C. Magnetofection-A highly efficient tool for antisense oligonucleotide delivery *in vitro* and *in vivo*. Mol Ther. 2003;7(5):700–10.
15. Sanchez-Antequera Y, Mykhaylyk O, Van Ti NP, Cengizeroglu A, De Jong HJ, Marshall W, Huston MW, *et al.* Magselectofection: an integrated method of nanomagnetic separation and genetic modification of target cells. Blood. 2011;117:e171–81.
16. Kami D, Takeda S, Itakura Y, Gojo S, Watanabe M, Toyoda M. Application of magnetic nanoparticles to gene delivery. Int J Mol Sci. 2011;12:3705–22.
17. Furlani EP, Ng KC. Nanoscale magnetic biotransport with application to magnetofection. Phys Rev E. 2008;77:061914.
18. Furlani EP. Nanoscale magnetic biotransport. In: Sattler K, editor. Handbook of nanophysics, nanomedicine and nanorobotics. Boca Raton: CRC Press; 2010.
19. Furlani EP. Particle transport in magnetophoretic microsystems. In: Kumar CSSR, editor. Microfluidic devices in nanotechnology: fundamental concepts. New York: Wiley; 2010. p. 215–62.
20. Furlani EP. Analysis of particle transport in a magnetophoretic microsystem. J Appl Phys. 2006;99(2):024912.
21. Gerber R. Magnetic filtration of ultra-fine particles. IEEE Trans Magn. 1984;20(5):1159–64.
22. Kelland DR. Magnetic separation of nanoparticles. IEEE Trans Magn. 1998;34(4):2123–5.
23. Fletcher D. Fine particle high gradient magnetic entrapment. IEEE Trans Magn. 1991;27(4):3655–77.
24. Davies LP, Gerber R. 2-D Simulation of ultra-fine particle capture by a single-wire magnetic collector. IEEE Trans Magn. 1990;26(5):1867–9.
25. Gerber R, Birss RR. High gradient magnetic separation. New Jersey: Wiley; 1983.
26. Gerber R, Takayasu M, Friedlander FJ. Generalization of HGMS theory: the capture of ultra-fine particles. IEEE Trans Magn. 1983;19(5):2115–7.
27. Takayasu M, Gerber R, Friedlander FJ. Magnetic separation of sub-micron particles. IEEE Trans Magn. 1983;19:2112–4.
28. Furlani EP, Ng KC. Analytical model of magnetic nanoparticle transport and capture in the microvasculature. Phys Rev E. 2006;73:061919.

29. Furlani EP, Sahoo Y. Analytical model for the magnetic field and force in a magnetophoretic microsystem. J Phys D: Appl Phys. 2006;39:1724–32.
30. Furlani EJ, Furlani EP. A model for predicting magnetic targeting of multifunctional particles in the microvasculature. J Magn Magn Mater. 2007;312(1):187–93.
31. Furlani EP, Sahoo Y, Ng KC, Wortman JC, Monk TE. A model for predicting magnetic particle capture in a microfluidic bioseparator. Biomed Microdevices. 2007;9(4):451–63.
32. Smith C-AM, Fuente J, Pelaz B, Furlani EP, Mullind M, Berry CC. The effect of static magnetic fields and tat peptides on cellular and nuclear uptake of magnetic nanoparticles. Biomaterials. 2010;31(15):4392–400.
33. Plank C, Scherer F, Schillinger U, Anton M, Bergemann C. Magnetofection: enhancing and targeting gene delivery by magnetic force. Eur Cells Mat. 2002;3 Suppl 2:79–80.
34. Furlani EP. Permanent magnet and electromechanical devices; materials, analysis and applications. New York: Academic; 2001.
35. Furlani EP. Computing the field in permanent-magnet axial-field motors. IEEE Trans. Mag. 1994;30.
36. Furlani EP. A method for computing the field in permanent-magnet axial-field motors. IEEE Trans Magn. 1992;28(5):2061–6.
37. Furlani EP. Field analysis and optimization of NdFeB axial field permanent magnet motors. IEEE Trans Magn. 1997;33 (5):3883–5.
38. Furlani EP, Knewtson MA. A three-dimensional field solution for permanent-magnet axial-field motors. IEEE Trans Magn. 1997;33 (3):2322–5.
39. Stratton JA. Electromagnetic theory. New York: McGraw-Hill; 1941.
40. Arfken G. Mathematical methods for physics, 3rd ed. California: Academic Press; 1985.